SAND2005-6685C

Dynamic Hohlraum Radiation Hydrodynamics

J.E. Bailey[1], G.A. Chandler[1], R.C. Mancini[2], G.A. Rochau[1], S.A. Slutz[1], M. Bump[5],
T.J. Buris-Mog[2], G. Cooper[1], G. Dunham[5], I. Golovkin[3], J.D. Kilkenny[4], P.W. Lake[1],
R.J. Leeper[1], R. Lemke[1], J.J. MacFarlane[3], T.A. Mehlhorn[1], T.C. Moore[5], T.J. Nash[1],
A. Nikroo[4], D.S. Nielsen[1], K. Peterson[1], C.L. Ruiz[1], D.G. Schroen[6], D. Steinman[4], and
W. Varnum[1]
1) Sandia National Laboratories, Albuquerque, N.M., 87185-1196
2) University of Nevada, Reno, NV
3) Prism Computational Sciences, Madison, WI
4) General Atomics, La Jolla, CA
5) K-tech Corporation, Albuquerque, N.M.
6) Schafer Corp., Livermore, CA

Z-pinch dynamic hohlraums are a promising indirect-drive inertial confinement fusion approach. Comparison of multiple experimental methods with integrated z-pinch/hohlraum/capsule computer simulations builds understanding of the hohlraum interior conditions. Time-resolved x-ray images determine the motion of the radiating shock that heats the hohlraum as it propagates toward the hohlraum axis. The images also measure the radius of radiation-driven capsules as they implode. Dynamic hohlraum LASNEX simulations are found to over-predict the shock velocity by ~20-40%, but simulated capsule implosion trajectories agree reasonably well with the data. Measurements of the capsule implosion core conditions using time- and space-resolved Ar tracer x-ray spectroscopy and the fusion neutron yield provide additional tests of the integrated hohlraum-implosion system understanding. The neutron yield in the highest performing CH capsule implosions is ~ 20% of the yield calculated with unperturbed 2D LASNEX simulations. The emissivity-averaged electron temperature and density peak at 900 eV and 4×10^{23} cm^{-3}, respectively. Synthetic spectra produced by post-processing 1D LASNEX capsule implosion simulations possess spectral features from H-like and He-like Ar that are similar in duration to the measured spectra. However, the simulation emissivity-averaged density peaks at a value that is four times lower than the experiment, while the temperature is approximately 1.6 times higher. The agreement with the capsule trajectory measurements and the ability to design capsule implosions that routinely produce implosion cores hot and dense enough to emit fusion neutrons and Ar spectra are evidence for a respectable degree of dynamic hohlraum understanding. The hohlraum shock velocity and implosion core discrepancies imply that calculations of the hohlraum radiation driving capsule implosions require further refinement.

I. Introduction

The dynamic hohlraum is an approach to Inertial Confinement Fusion (ICF) [1] that is interesting because a large amount of x-ray energy can be coupled to a capsule. This type of hohlraum is created by accelerating an annular tungsten z-pinch plasma radially-inward onto a cylindrical low density CH_2 foam placed at the z-pinch axis. The collision launches a radiating shock that propagates toward the cylinder axis. Radiation from the shock is trapped by the tungsten z-pinch plasma, forming a hohlraum that can be used to implode ICF capsules. Experiments conducted at the Sandia National Laboratories Z facility [2-4] have coupled approximately 40 kJ of x-rays to a 2 mm diameter capsule, about one quarter the energy in point designs of capsules intended to reach ignition on the future National Ignition Facility (NIF) [1,5]. The absorbed energy in Z capsule experiments is approximately 20x higher than in previous laser driven hohlraum experiments at NOVA [1,6]. The ~220 eV peak temperature is similar, but the longer duration and larger size of the Z dynamic hohlraum enable implosion experiments with capsules that are typically 5x larger in radius. Z dynamic hohlraum implosion experiments might therefore serve to advance ICF implosion physics as the absorbed energy and capsule size are scaled up, in addition to the role such experiments play in evaluating the prospects for reaching ignition or high yield with a dynamic hohlraum on a future pulsed power facility.

ICF has several requirements, in addition to large capsule absorbed energy and high drive radiation temperatures. These requirements include detailed control over the drive radiation symmetry and over the drive radiation history. The ability to advance ICF science in general and the possibility of future ignition and high yield dynamic hohlraum implosions both depend on whether the symmetry and drive radiation can be measured, understood, and controlled accurately enough. The first key question is whether an accurate picture for formation and evolution of a basic dynamic hohlraum can be developed. Here, a basic dynamic hohlraum is defined to consist of a CH_2 cylindrical foam radiation converter and a single-atomic-species high-Z cylindrical z-pinch plasma. An appealing feature of the dynamic hohlraum is design flexibility: advanced designs employing modifications such as radiation shields, mid-Z doped foams, and shaped quasi-spherical hohlraums could offer the potential to tailor the radiation field at the capsule. In this paper we describe progress toward the development and validation of basic dynamic hohlraum physics understanding that is a prerequisite to pursuing more advance designs.

The z-pinch dynamic hohlraum concept [2, 7-8] was independently invented by several research groups working in the early 1980s. Initial design studies were performed, but, to the best of our knowledge, more than a decade passed before significant experimental evaluations were made. In the mid 1990s, high hohlraum temperatures were reported, first [9] at the ANGARA V facility in Russia and then at the SATRUN and Z facilities in the United States [10-13]. The work at Saturn and Z emphasized the use of high radiation flux emerging from the dynamic hohlraum end as a source for radiation science experiments. Building on this effort, larger dynamic hohlraums were created at Z that reached radiation drive temperatures of approximately 135 eV in a ~ 10 mm diameter, 15 mm tall hohlraum [14]. These temperatures were too low to perform significant capsule implosion experiments, but substantial progress was made in simulating and measuring the dynamic hohlraum radiation hydrodynamics [15-16]. This improved capability and understanding led to the creation of somewhat smaller dynamic hohlraums with radiation drive temperatures of approximately 200 eV in a ~ 6 mm diameter 12 mm tall hohlraum [17]. These hotter hohlraums were used to successfully drive capsule implosions that produced an implosion core hot and dense enough to produce measurable x-rays [18] and neutrons [19-20].

The strategy followed in the experiments described here was to employ both direct hohlraum measurements and measurements of the capsule response to the radiation in order to build a comprehensive system understanding. We need benchmarked simulation predictions of radiation drive at the capsule in order to understand the system well enough that it could be scaled up to reach ignition and high yield on a future larger facility. Simulations are also required because, as in all indirect drive experiments, it is difficult or impossible to directly measure the drive radiation temperature (T_r) at the capsule. The simulation T_r predictions depend on several complex issues, including run-in radiation alteration of the foam radiation converter, z-pinch plasma momentum, current diffusion through the z-pinch, simulation zoning, z-pinch instabilities, and hot plasma opacities (tungsten and CH). The complexity dictates that a number of techniques should be employed. The direct hohlraum measurements described here emphasize shock hydrodynamics and reproducibility diagnosed by recording time-resolved snapshots of the shock self emission using an x-ray framing camera. Measurements of the radiation emerging from the hohlraum end and local interior conditions determined from spectroscopy of Si tracer atoms added to the foam [21] will be described elsewhere. The implosion experiments described here were aimed at measuring the drive radiation symmetry and at testing the fidelity of simulation drive temperature. Symmetry measurements using the “symmetry capsule” technique [22] will be described elsewhere. The simulation drive temperature fidelity was tested by measuring the implosion trajectory of a capsule using self backlit images. An additional test was performed by examining whether core temperature and density agreed with measurements obtained by recording time resolved spectra from Ar tracer atoms in the implosion core. A complete evaluation of these results is not yet available. However, they suggest that modest adjustments (at about the 10-15% level) are needed to bring the simulation drive temperature into agreement with experiment. Considering that the simulations treat the z-pinch, hohlraum, and capsule as an integrated system, beginning with the z-pinch current and modeling the experiment over a ~100 nsec period up to and including the capsule implosion, this is respectable agreement.

II. Experiment

The nested tungsten wire array z-pinch plasmas used to create dynamic hohlraums at the Z facility implode over approximately 98 nsec from initial diameters of 4 cm and 2 cm for the 240-wire outer and 120-wire-inner arrays, respectively (Fig. 1). The array heights are 12 mm. Current from the Z pulsed power generator is injected into the wire array assembly, reaching a ~20 MAmp peak in ~100 nsec. The wire diameter is 7.5 microns, chosen so that the wire plasma mass is similar to the foam mass. This wire array configuration was selected because it is very similar to configurations previously developed in experiments aimed at maximizing the radiation power that exits the top diagnostic aperture for radiation science applications [10-13]. This configuration has not been experimentally optimized for use in ICF implosion experiments, but it does have several positive features. The drive temperature at the capsule is clearly adequate to create hot and dense capsule implosion cores [18-20]. In addition, the 40-mm-initial-diameter nested array configuration used here appears to possess minimal contributions from early wire ablation, precursor plasma formation, and trailing mass that complicate the implosion of smaller diameter, smaller wire number arrays.

The capsules used in these experiments were constructed at General Atomics Corp. They consisted of a 2mm inner diameter $CH_{1.3}$ shells with specifications that have evolved over the ~ three year period of these experiments. Typically, the shell consisted of a ~ 30 μm inner GDP layer, a 4 μm poly vinyl alcohol (PVA) layer, and a 10-50 μm outer GDP layer (Fig. 2a). The PVA layer provides a permeation barrier that prevents the D_2 fill gas from leaking out of the capsule during the 1-3 day preparation period leading up to each Z implosion experiment. The PVA was located in the middle of the shell in an attempt to mitigate the wall thickness variations caused by PVA thickness variations and also to protect the PVA from exposure to ambient air. The fabrication of uniform thickness PVA layers is a formidable challenge. This challenge has been even more difficult because, when initial targets were made, no detailed shell wall measurements were feasible. Until recently, the best integrated characterization of the PVA uniformity was provided by measurements of the half life for the D_2 fill gas to leak out of the shell. Initial coatings had large wall thickness variations that led to D_2 fill gas leakage half lives of typically 3-10 days. This led us to overcoat the shell with 0.8-1.6 μm Al layer. Preliminary measurements indicated the Al overcoat provided up to twice the half life for the D_2 fill gas. More recent experiments were conducted with improved targets that provided a D_2 fill gas half life of up to 30 days without any need for the supplemental Al coating. Simultaneously, automated high resolution x-ray radiography measurements of the capsule wall thickness variations over a single great circle around the capsule became available (Fig. 2b). These measurements show that wall thickness variations of ± 2 microns persist, even for the highest performing capsules.

The fill gas is introduced into the shell by placing the shell into a vacuum system, heating up the shell to remove background gases and air, then pressurizing the chamber with the desired amounts of Ar and D_2. The total gas pressure is measured by weighing the shells. As mentioned above, there are concerns that the fill gas may leak out of the capsule during handling as it prepared for the Z experiment. To monitor this possibility a second (“buddy”) capsule with similar characteristics is prepared in exactly the same way as the capsule to be used on Z. After the experiment, the “buddy” capsule fill gas composition is measured by bursting the capsule inside a vacuum chamber equipped with a high resolution mass spectrometer. This test reveals whether any residual contaminant gases were introduced during the original filling procedure, as well as whether the actual leak rate under handling was the same as the original estimate.

The foam/target assembly is fabricated by casting the capsule in the center of a 14 mg/cc CH_2 (TPX) foam. The foam diameter was 6 mm and the height was 12 mm. These specifications were determined using theoretical calculations [17] benchmarked against previous experiments conducted with 10 mm diameter 5 mg/cc foams. Smaller diameter foams generally provide a higher radiation drive, but the dwell time of the radiation prior to the arrival of the converter shock on axis is shorter. TPX foam at this density consists of essentially solid density CH_2 inter-tangled strands with ~ 20 micron voids. The voids are believed to rapidly transform into plasma as the foam is heated by the z-pinch x-rays, but the complexity of this process introduces some uncertainty into the early phase ablation of the foam. The capsule placement and foam uniformity can both be influenced by the foam casting process. Side-view and end-view radiographs are recorded using a Cr-anode x-ray source to generate a point-projection image on the face of a x-ray CCD camera (Fig. 3). Typical capsule placement accuracy is within 100 microns of the foam center. The foam density is determined after casting by measuring the foam volume and weighing. After the capsule foam target has been characterized it is sometimes frozen for 2-10 days prior to use in a Z experiment. Freezing allows targets to be assembled ahead of experiment scheduled date, while greatly reducing capsule fill gas leakage and foam shrinkage. The foam is attached to the top of the wire array assembly using a few drops of ultraviolet cured epoxy. Note that the large size of the foam makes even a 1 degree tilt angle of the foam significant, since it corresponds to a ~100 μm offset of the capsule away from the z-pinch axis.

The principal diagnostics employed in these experiments included x-ray spectrometers, x-ray pinhole cameras, neutron time of flight and activation detectors, x-ray diodes (XRD), and diamond photo-conducting diodes (PCD). Descriptions of these diagnostics are available elsewhere [23-24]. The x-ray power emerging from the top diagnostic aperture (at 6° with respect to the z-pinch axis) and from the side of the z-pinch (at 78° with respect to the z-pinch axis) were measured with arrays of filtered XRDs and PCDS [25-27]. The neutron energy spectrum was measured with scintillator-photomultiplier tube time-of-flight detectors located to the side and below the target [19-20]. The neutron yield was determined with an array of In, Be, and Pb activation detectors.

Here, we emphasize x-ray spectroscopy and imaging measurements. X-ray spectroscopy measurements of Ar tracer atom emission from the hot implosion core were performed with two or three time- and space-resolved elliptical crystal spectrometers (TREX) [28]. One spectrometer viewed the capsule along the polar axis (Fig. 1). The other spectrometers viewed the capsule from the side at a 12° angle with respect to the equatorial plane. These spectrometers used an array of six space-resolving slits to project spectrally-resolved images of the capsule onto six time-gated microchannel plate (MCP) striplines. The time resolution in early experiments was ~ 1 ns and was improved to ~ 350 ps in recent work. The spatial resolution was ~ 50-85 μm. The distance from the source to the pentaerythritol crystals is 2.92 m and 4.10 m for the top viewing and side viewing spectrometers, respectively. The spectral range was approximately 1.3 Angstrom and the spectral resolution was $\lambda/\delta\lambda \sim 800$-1000, depending on the wavelength. The data are recorded on Kodak TMAX film and the film response was unfolded using a step wedge. We account for the relative instrument sensitivity using Ref. [29-30], as an actual calibration was unavailable. Implosion core x-ray spectra were recorded on several space-resolved time-integrated spectrometers, in addition to the time-resolved TREX instruments.

X-ray imaging measurements of the foam converter shock and the capsule implosion were performed with an eleven-frame time-gated x-ray pinhole camera located at 0° with respect to the z-pinch axis. In most of the experiments reported here the pinhole camera was located below the target and the TREX1 spectrometer was located in the 0° location on top. In some experiments the pinhole camera was located on top and the bottom diagnostic aperture was plugged with a gold-coated steel plate. The top diagnostic aperture diameter was 4-4.5 mm and the bottom aperture diameter was 4-8 mm, depending on the experiment. The full width at half maximum for each pinhole frame and the interframe time were ~ 0.5-1.0 ns. The interframe time accuracy was estimated to be ± 50 ps and the image timing accuracy with respect to the x-ray power measurements was approximately ± 300 ps. The pinhole array consists of 22 pinholes projecting two images onto each of 11 MCP striplines. The pinhole diameter was 50-75 μm. Typically, one pinhole image on each frame used a 4-μm kimfol filter to record an image dominated mainly by 250 eV photons and a second thicker filter to record an image dominated by > 800 eV photons. The magnification was 0.66 and the spatial resolution was ~200 μm.

III. Hohlraum imaging results

Images of the self-emission emerging from the hohlraum end are valuable because they provide measurements of the foam converter shock trajectory, the shock velocity, and the shock symmetry [14]. In addition, the spatial profiles of the self emission are sensitive to the radiation temperature inside the hohlraum and the radiation cooling rate behind the shock [16]. A set of images obtained with the top-viewing camera is shown in Fig. 4. The shock self-emission radius, annular width, and intensity as a function of azimuthal angle are measured from each snapshot by taking radial direction lineouts over a set of azimuthal angles. The spacing between lineouts is typically 10 degrees. The center of the self-emission image is located by iteratively finding the image position that minimizes the deviation of the radius with respect to the mean radius. The standard deviation of the radius is typically ~2-4 %, indicating a high degree of shock azimuthal uniformity. This deviation includes both measurement error and whatever real deviation from circularity exists. The shock trajectory (shock radius as a function of time) is valuable because it can be used as a timing fiducial to relate one experiment to another, or simulations to experiments. This is similar to using laser timing in laser heated hohlraum experiments, since the shock radiation is responsible for heating the dynamic hohlraum. The shock trajectory is also important since in present radiation-driven capsule experiments we prefer to avoid the complexities introduced if the shock arrives at the axis prior to completion of the implosion. Note that allowing the shock to approach the axis in future more-aggressive experiments may be desirable [31]. In this case the radiation temperature can be substantially higher and it is not clear whether the shock arrival harms the implosion, since the capsule ablation plasma pressure may be sufficient to hold off the shock.

The shock velocity is determined by fitting the trajectory data, using the standard deviation about the mean radius at each time as an estimate for the radius uncertainty. The interframe timing uncertainty is neglected in these fits and the true velocity uncertainty may be somewhat larger. The present data are consistent with a constant velocity with time, although there are suggestions that the initial velocity is slightly lower and the shock speeds up with time. The velocity determined from linear fits to individual experiments ranges from 283 μm/ns to 398 μm/ns, with uncertainties between ±2-14% (Fig. 5a). The uncertainty obtained in a given experiment depends strongly on the number of frames recorded, which can vary from two to ten. In particular, fits to experiments with only three or four measurements can be strongly biased by errors in either the first or last data point. We therefore used a statistical averaging procedure to determine the velocity from the ensemble of experimental data, under the assumption that the velocity is the same. This procedure entailed first determining a weighted mean velocity from thirteen individual Z experiments. Next, the trajectory data from each experiment was time shifted to minimize the difference between the measured trajectory and the trajectory corresponding to a constant velocity at the weighted mean value (Fig. 5b). For convenience, the trajectory corresponding to the weighted mean was adjusted so that it intersects the time axis at t=0. The velocity determined by a linear fit to the entire data set is 325 μm/ns ± 1%. The validity of assuming the velocity is the same in all experiments is supported by examining the distribution of the data about the fit. The chi-squared of the fit to the ensemble is 1.2, indicating that the data are consistent with a 325 μm/ns velocity that is constant over time and between experiments to within ± 1 %. However, we cannot preclude the possibility that some real velocity differences exist between experiments. Approximately 70% of the individual measurements are within ± 12% of the 325 μm/ns ensemble-average velocity. Therefore, the true velocity is within ± 12% of the ensemble fit result at the 1σ confidence level and it may be much closer. It is interesting that the velocity is essentially the same as the measured velocity in previous experiments using larger (10 mm diameter) lower-density (5 mg/cc) dynamic hohlraums, within the experiment uncertainty.

The circularity and narrow annular width of the shock both indicate that the shock is symmetric. Plots of the shock radius as a function of angle possess a degree of circularity similar to results for low-density large-diameter dynamic hohlraums displayed in Ref. [14,16]. The radius is constant to within better than ± 2-4 %. The annular width of the shock is typically 300 μm ± 15% . This is approximately equal to the convolution of the instrument resolution and the motional blurring caused by the high shock velocity and the finite camera gate time. Therefore, the actual annular width is less than approximately 200 μm. The annular width is sensitive to the shock asymmetry (see Ref. 16) because the instrument collects photons from a significant fraction of the entire foam height. Calculations indicate that the foam optical depth in the 250-1000 eV photon range used for the imaging measurements is small compared to the foam height, an expectation consistent with imaging measurements that successfully recorded images of a Be marker embedded in the foam [32]. The narrow annular width implies that corrugations in the shock along the height of the foam are small enough that they broaden the shock annular width by less than 200 μm. Such corrugations might be caused, for example, by magnetic

Rayleigh-Taylor instabilities that create mass density modulations in the tungsten z-pinch plasma prior to the impact between the z-pinch and the foam. The negligible effect of instabilities on the shock in a similar DH configuration was found in Ref. 16 to be explained by damping of the instability amplitude as the z-pinch plasma sweeps up the rarified foam plasma that was ablated during the run-in phase. This instability mitigation greatly reduces one of the main concerns for the DH ICF approach, although the possibility still exists that instabilities might lead to randomly varying leaks in the tungsten plasma hohlraum radiation case.

The shock emission intensity typically varies with azimuthal angle by a substantial amount in comparison with the relatively-constant shock radius (Ref. []). Possible contributions to the intensity variations include shock pressure variations, foam inhomogeneities, and inhomogeneous diagnostic aperture filling by tungsten. The first explanation appears unlikely, since the intensity variation often persist over time. If an azimuthal shock pressure variation persisted over time it would imply that a velocity variation should also persist. A persistent velocity variation would cause a growing deviation from circularity, which is not observed. Work is in progress to use the measured shock circularity to place an upper bound on the shock intensity variation that might be due to shock pressure variation.

IV. Capsule imaging

The Figure 4 images are suitable for determining the capsule trajectory in addition to the shock trajectory [14]. The capsule used in this relatively-early experiment was a 1.6-mm-inner-diameter 50-μm-thick CH shell filled with 2.6 atm CD_4 + 0.085 Atm Ar.The hohlraum design was identical to the other experiments described here. The capsule image is formed by a convolution of thermal radiation originating from above and below the capsule with the self emission from the capsule ablation plasma. The capsule shell absorbs the thermal radiation from below the capsule, forming a self-backlit image of the capsule implosion. The capsule ablation plasma emission appears as a limb-brightened ring around the capsule. Note the intensity scale in each Fig. 4 frame has been normalized. The shock converges onto the pinch axis as the slightly-off-axis capsule implodes. The capsule absorption does not appear in images prior to approximately t=-6 ns (not included in Fig. 4), presumably because the radiation temperature is low and the foam optical depth is high.

The capsule diameter as a function of time was measured from lineouts taken through each image every 18 degrees. The angle-averaged-diameter was divided by 2 in order to determine the capsule radius (Fig. 5). The uncertainty is dominated by the image interpretation when the ablation plasma emission, the thermal radiation, and the shock emission begin to compete. The radius measurements corresponding to the first six points are the result of analyzing the last six frames of data acquired in experiment z882. The final radius/time measurement was obtained from another experiment (Z860) that employed a nominally identical capsule. In this experiment, the capsule implosion core self emission was visible together with the foam shock (see Fig. 6 in Ref 17). The relative timing between these experiments was determined using the measured shock diameter, as the high accuracy of the fit to the ensemble of shock trajectory data points is regarded as providing the most accurate timing between these experiments.

1-D capsule implosion computer simulations [17,33] were performed to evaluate the self-consistency of the calculated radiation temperature, shock trajectory, and the capsule radius evolution in response to the radiation. The Lagrangian simulations computed the implosion of a spherical capsule embedded in spherical foam. The calculated shock velocity is higher than the experiment. This renders the relative timing between the simulations and experiments somewhat subjective. Nevertheless, the calculated capsule radius, obtained by post-processing the simulations, agreed reasonably well with the measurements (Fig. 6). The data may suggest that the simulation foot is too low, since the capsule appears to begin moving earlier in the experiment. The data supports the reasonableness of the simulation results, while also demonstrating further improvements are needed.

V. Capsule Core Temperature and Density

The implosion core electron temperature (T_e) and density (n_e) depend on the drive radiation time history. Therefore, T_e and n_e measurements can be exploited as an integrated test of simulation drive temperature predictions. In addition, a key to ICF is the ability to tailor the spatial profiles of the temperature and density in the implosion core hot spot. A goal of our research is to develop the ability to measure the time-resolved T_e and n_e spatial profiles. The core conditions are diagnosed using time- and space-resolved spectroscopy measurements of Ar tracer atom emission and time- and space-integrated neutron spectroscopy and yield measurements. The neutron measurements (Fig. 7a) provide strong evidence that a hot and dense implosion core is produced [19]. The DD yield has increased from initial ~5×10^9 values obtained with 1.6-mm-diameter 50-μm-wall capsules to ~ 2-3 $\times 10^{11}$ in recent experiments with 2-mm-diameter 70-80 μm thick walls. This increase is due to a combination of improved fabrication techniques, increased capsule diameter, and thicker capsule wall. The yield uncertainties are estimated to be $\pm$ 15%The measured yields in the highest performing CH capsule experiments are within 20-30% of predictions obtained with integrated 2D z-pinch/hohlraum/capsule simulations (Fig. 7b). The remaining discrepancy may arise from drive temperature differences, mix, and asymmetries. Further analysis is required to determine the relative influence of these and other processes on the experiment neutron yield.

A set of x-ray spectra obtained in an experiment using a 2-mm-diameter 70 micron CH wall capsule filled with ~ 25 atm D_2 + 0.085 atm Ar is shown in Figure 8. In this experiment we acquired spectra from two TREX spectrometers (TREX5 and TREX6), both positioned to the side of the target at a 78 degree angle with respect to the z-pinch axis. The time resolution in this experiment was ~ 350 psec and the spatial resolution was ~ 85 μm. The TREX5 spatial resolution direction was horizontal (along the equator) and the TREX6 spatial resolution direction was vertical (along the polar axis). This orthogonal spatial slit orientation implies that the spectra can in principle be inverted to provide a tomographic reconstruction of the 2D spatial profiles of the temperature and density. Work is in progress to obtain three simultaneous views to further strengthen such reconstructions.

The analysis methods used to infer temperature and density from the measured spectra begins by correcting the data for the measured film response, removing spatial warping caused by crystal imperfections, applying the wavelength scale, and correcting for the instrument efficiency. In each time-resolved frame we take both a space-averaged lineout and a set of space-resolved lineouts. The space-average lineout is useful [18] for determining the average hot spot conditions as a function of time from the data (Fig. 9). A number of different analysis approaches have been developed to infer temperature and density from the spectra. These include:

1) An Interactive Data Language (IDL) based method that provides semi-automated extraction of line intensities and widths from the data. Then alibrary of single n_e,T_e,ρr plasma calculations performed with the PRISMSPECT [34] atomic and plasma model is used to determine T_e and n_e from the intensities and widths.

2) A method that fits synthetic spectra to specific portions of a spectrum using the UNIFORM2 code (Ref. [35]). Typically, the most optically thin region from Heβ to Lyγ is chosen. As with method (1), an estimate of the plasma ρr is required in order to account for opacity effects.

3) The line of best fit (LOBF) method [36] self-consistently determines n_e and ρr independently for the H-like and He-like Ar populations by fitting the Lyα, Lyβ, Lyγ and Heα, Heβ, and Heγ Stark- and opacity-broadened line profiles [37].

4) Fits to the complete spectrum using the ROBFIT line fitting code [38] to determine the line intensities and widths. This has the advantage that uncertainties in the fitted quantities are determined. As with method (1), a library of PRISMSPECT calculations is then used to infer the plasma conditions

We consider the combination of the LOBF and ROBFIT methods to be the most powerful and complete methods available to us. However, they are also the most time consuming to implement. Consequently, the analysis of the Z1467 experiment presented here must be considered work in progress. Despite this present limitation, the data already provide some conclusions regarding the capsule implosion physics.

Time-resolved spatially-averaged measurements from the Z1467 TREX5 data presented in Fig. 8&9 are shown in Fig. 10. The spatial average data are analyzed under a uniform plasma approximation. This approximation is a useful starting point for building understanding of the implosion core physics, while developing and implementing methods designed to take advantage of the space-resolved measurements that are available. The temperature is determined using the UNIFORM2 fitting code to fit the Heβ – Lyγ spectral region. The electron density is determined by applying the LOBF method to fit the H-like and He-like Ar line sequences. The density is higher for the He like emission than for the H-like emission, a typical result in our analysis of Z capsule implosions. This observation is probably due to the fact that, even though we assume a uniform core plasma, the relative emission intensity from different parts of the core for each spectral line is weighted by the line emissivity and further modified by the plasma opacity as the line propagates to the edge of the plasma. ICF implosion plasmas are often expected to reach pressure equilibrium in which the hottest central region has a lower density and the cooler periphery [39,40] has a relatively higher density. The Z implosion results appear to be consistent with this expectation.

Maximizing the understanding provided by the results requires comparison with simulations. A rigorous comparison is not trivial because of the emissivity weighting and opacity modifications mentioned above. This comparison is accomplished here by post-processing results obtained with 1D LASNEX simulations using an atomic model that includes a detailed treatment of Li-, He-, and H-like Ar. The model uses a collection of pre-calculated Stark broadened line profiles that include ion dynamics effects for Ar embedded in D_2 plasma. The level populations are calculated self-consistently with the radiation, under the escape factor approximation. Opacity effects on the emergent line profiles and intensities are included, as are satellite transitions with spectator electrons in the principal quantum number =2,3 levels. For the calculations presented here, the free-bound recombination continuum was not included, although it has been implemented in a more recent version of the post-processing routine. The postprocessing produces synthetic spectra for the calculated plasma conditions. The spectra can be computed either for spatially-resolved or spatially-averaged lineouts. The space average result is essentially subject to the same uniform plasma approximation employed in the experiment analysis.

A collection of synthetic spectra at times roughly corresponding to the spatial-average lineouts from the Z1467 experiment are shown in Fig. 9. The simulation results include emission that are qualitatively similar in many respects to the experimental results. In particular, the duration of the emission is about the same and bright features from H-like and He-like are predicted. However, there are also some important differences. Specifically, the experiment lines are all substantially broader, indicating higher density. In addition, the simulation spectra are somewhat overionized compared to the data.

Quantitative comparisons of the simulations and measurements can be obtained by applying the same analysis methods to the synthetic spectra as the data. The density and temperatures obtained with the LOBF and UNIFORM2 methods are shown in Fig.10. The relative timing of the simulations and measurements was determined in this case by shifting the simulations so that the Lyβ line intensity peaks at the same time. The simulation electron density is approximately a factor of four lower than the measurement. The simulation electron temperature is a approximately a factor of ~1.5 higher. Possible reasons for these differences are discussed below.

VI. Discussion

Evidence supporting the reasonableness of the dynamic hohlraum basic picture is provided by good agreement between measurements and simulations of the capsule trajectory as it implodes in response to the radiation. The sensitivity of the trajectory to variations in $T_r(t)$ must be studied in order to fully exploit this technique and place quantitative bounds on $T_r(t)$. Further evidence for the basic picture validity is supplied by the ability to design capsule implosions that produce both DD fusion neutrons and Ar tracer emission spectra.

On the other hand, the simulation shock velocities are higher than the measured value, indicating the hohlraum is driven with a higher pressure shock in the simulation. It is worth recalling that the predicted shock velocity in larger, lower-density dynamic hohlraums agreed well with the measured value. The confidence inspired by the excellent agreement with the large low-density hohlraum measurements motivated the smaller hohlraum designs employed here to produce higher temperature hohlraums. There is little doubt that the smaller hohlraum did indeed produce higher temperatures, since capsule implosions producing fusion neutrons and Ar tracer emission are now routine. However, the fact that the shock velocity did not increase indicates that further refinements to the simulation physics are needed. Work is in progress to quantify the hohlraum temperature reduction that would be suggested by the lower shock velocity, as well as to identify the phenomena that lead to simulation predictions of higher shock velocity in the 6-mm-diameter dynamic hohlraum.

The most straightforward explanation for the difference in the simulated and measured implosion core conditions is that the drive temperature history in the experiment is different. The diagnostic capsules used here are deliberately designed with a relatively thin ablator that burns through when the implosion is partially complete. A qualitative expectation is that if the capsule remains ablative in the experiment longer than expected, the core density will increase. This could result, for example, from a higher T_r foot, a slower T_r rise, a lower T_r peak, or a combination of these possibilities. Work is in progress to quantitatively evaluate how different $T_r(t)$ would have to be to explain the core density discrepancy, but preliminary calculations suggest that a modest ~ 10-15% changes might be sufficient. Other processes that might also contribute to this discrepancy, including mix and radiation cooling effects, are presently considered less likely but are still under active consideration.

In summary, an accurate predictive capability for the drive temperature $T_r(t)$ experienced by a capsule is an essential goal for dynamic hohlraum driven ICF. This goal is challenging because $T_r(t)$ is influenced by many processes that are each complex. The strategy employed in our research is to use multiple measurements in order to both identify deficiencies in our understanding and to determine the underlying physics improvements needed to further strengthen the predictions. In addition to the measurements described here, measurements of the radiation power emerging from the dynamic hohlraum end and of Si tracer spectral emission from the hohlraum interior are both expected to provide further constraints on the hohlraum physics model. This research is a foundation for high-precision dynamic hohlraum inertial fusion science experiments.

Acknowledgement

We thank the Z accelerator, diagnostics, materials processing, target fabrication, and wire array teams for invaluable and dedicated technical assistance. We also thank the General Atomics Inc. team that fabricated the capsules. S. Balsley and H. Peebles measured the capsule fill gas composition and L.P. Mix provided data processing assistance. We are also grateful to J.P. Qunitenz, J.L. Porter, and M.K. Matzen for support and encouragement. Sandia is a multiprogram laboratory operated by Sandia Corporation, a Lockheed Martin Company, for the U.S. Dept. of Energy under contract No. DE-AC04-94AL85000.

References

1. J. Lindl, Phys. Plasmas 2, 3933 (1995).
2. M.K. Matzen, Phys. Plasmas 4, 1519 (1997).
3. R. Spielmann, C. Deeney, G. A. Chandler, M. R. Douglas, D. L. Fehl, M. K. Matzen, D. H. McDaniel, T. J. Nash, J. L. Porter, T. W. L. Sanford, et al., Phys. Plasmas **5**, 2105 (1998).
4. C. Deeney, M.R. Douglas, R.B. Spielman, T.J. Nash, D.L. Peterson, P. L'Eplattenier, G.A. Chandler, J.F. Seamen, and K.W. Struve, Phys. Rev. Lett. **81**, 4883 (1998).
5. NIF ignition design
6. B.A. Hammel, C.J. Keane, M.D. Cable, D.R. Kania, J.D. Kilkenny, R.W. Lee, and R. Pasha, Phys. Rev. Lett. 70, 1263 (1993).
7. V.P. Smirnov Plasma Phys. Control. Fusion 33, 1697 (1991).
8. J.H. Brownell, R.L. Bowers, K.D. McLenthan, and D.L. Peterson, Phys. Plasmas 5, 2071 (1998).
9. Angara result
10. T.W.L. Sanford et al., Phys. Plasmas 7, 4669 (2000); T.W.L. Sanford et al., Phys. Plasmas 9, 3573 (2002).
11. T.J. Nash et al., Phys. Plasmas 6, 2023 (1999).
12. D.L. Peterson et al., Phys. Plasmas 6, 2178 (1999).
13 Sanford recent PRL
14. J.E. Bailey et al., Phys. Rev. Lett. 89, art# 095004 (2002).
15. S.A. Slutz et al., Phys. Plasmas 8, 1673 (2001).
16. R.W. Lemke, J.E. Bailey, G.A. Chandler, T.J. Nash, S.A. Slutz, and T.A. Mehlhorn, Phys. Plasmas 12, 012703 (2005).
17. S.A. Slutz et al, Phys. Plasmas 10, 1875 (2003).
18. J.E. Bailey et al., Phys. Rev. Lett. 89, art# 085002 (2004).
19. C.L. Ruiz et al., Phys. Rev. Lett. 89, art# 015001 (2004).
20. R.J. Leeper et al, Proc IFSA
21. J.E. Bailey Jour. HEDP
22. A. Hauer et al., Rev. Sci. Instrum. 66, 672 (1995).
23. R.J. Leeper et al., Nucl. Fusion 39, 1283 (1999).; T.J. Nash et al., Rev. Sci. Instrum. 72, 1167 (2001).
24. Recent Z diagnostics overview
25. G.C. Idzorek and R.J. Bartlett EUV, X-ray, and Gamma-Ray Instrumentation for Astronomy VIII, ed. by OHW Siegmund and MA Gummin: SPIE Proc. V. **3114**, p. 349, 1997.
26. G.A. Chandler, C. Deeney, M. Cuneo, D.L. Fehl, J.S. McGurn, R.B. Spielman, J.A. Torres, J.L. McKenney, J. Mills, and K.W. Struve, Rev. Sci. Instrum. **70**, 561 (1999).
27. R.B. Spielman, L.E. Ruggles, R.E. Pepping, S.P. Breeze, J.S. McGurn, and K.W. Struve, Rev. Sci. Instrum. **68**, 782 (1997).
28. P.W. Lake Rev. Sci. Instrum. **75**, 3690 (2004).
29. B.L. Henke, H.T. Yamada, and T.J. Tanaka, Rev. Sci. Instrum. 54, 1311 (1983); B.L. Henke, Private Communication.
30. Landen MCP response
31. J.S. Lash et al., C.R. Acad. Sci. Paris 1, 759 (2000).
32. G.A. Chandler et al, to be published

33. G. Zimmerman and W. Kruer, Comments Plasma Phys. Control. Fusion 2, 85 (1975).
34. J.J. MacFarlane, P.R. Woodruff, and I.E. Golovkin, “SPECT3D Imaging and Spectral Analysis Suite”, Prism Computational Sciences Report No. PCS-R-045, Madison, WI, 53711, 2003 (unpublished).
35. R.C. Mancini et al, to be published.
36. J.D. Kilkenny, R.W. Lee, M.H. Key, and J.G. Lunney, Phys. Rev. A 22, 2746 (1980).
37. . L.A. Woltz and C.F. Hooper Jr., Phys. Rev. A 38, 4766 (1988); R.C. Mancini, D.P. Kilcrease, L.A. Woltz, C.F. Hooper Jr., Comp. Phys. Commun., 63, 314 (1991); D.A. Haynes, D.T. Garber, C.F. Hooper Jr., R.C. Mancini, Y.T. Lee, D.K. Bradley, J. Delletrez, R. Epstein, and P. Jaanimagi, Phys. Rev. E 53, 1042 (1996).
38. ROBFIT
39. I. Golovkin et al., Phys. Rev. Lett. 88, art# 045002 (2002); L.A. Welser et al., J. Quant. Spectrosc. Radiat. Transfer 81, 487 (2003).
40. S.P. Regan et al. Phys. Plasmas 9,1357 (2002); S.P. Regan et al., Phys Rev Lett. 89, 085003 (2002).

Figure Captions:

1. Dynamic hohlraum schematic diagram. Voltage applied across the top and bottom electodes causes current to flow through the wire arrays. The magnetic pressure accelerates the wire plasma onto the CH2 foam, forming a hohlraum.

2. A typical capsule cross-section is shown in (a). The radial dimensions are in microns. The fill pressure is nominally 12-25 atm D2 +0.085 atm Ar. The plot in (b) is a measurement of wall thickness variations characteristic of the best CH/PVA capsules used in these experiments.

3. Side-view and end-view radiographs of the target assembly used in the Z1467 experiment.

4. Time-resolved x-ray images obtained in experiment Z882. The capsule was a 1.6-mm-inner-diameter 50-micron-thick CH/PVA shell filled with 2.6 atm CD4 + 0.085 atm Ar. Each plot is a horizontal lineout through the corresponding frame. The lineout intensities are in arbitrary units, scaled to optimize the visibility of the features in each snapshot.

5. The foam shock velocity (a) inferred from x-ray images similar to Fig. 4, acquired in thirteen separate Z experiments. The solid line is the most probable value obtained by computing a weighted mean for the data. The dashed lines are the 1s uncertainties in the weighted mean. The trajectory plot in (b) is the ensemble of the 60 measurements obtained in the 13 experiments displayed in (a). The red line is the trajectory corresponding to the weighted mean velocity, defined such that t=0 corresponds to the shock arrival at the axis. The collection of data from each experiment was time shifted to minimize the difference with the mean velocity trajectory.

6. Comparison of post-processed simulations with the trajectory measurements obtained in experiments with 1.6-mm-ID 50-mm-thick CH wall capsules. The red dots are the measured shock velocity, time shifted to the weighted mean velocity trajectory (red dash). The green dots are the measured capsule trajectory. The blue, red, and green lines are post-processed simulation results for the radiation temperature at the capsule, the foam shock trajectory, and the capsule trajectory, respectively.

7. Neutron time-of flight measurements (a) from detectors at different distances confirm that the neutron energy is consistent with DD thermonuclear neutron production. The ratio of the measured and 2D unperturbed simulated yield for the best performing CH wall implosions is 20-30% (b).

8. Time-and space-resolved Ar emission spectra from experiment Z1467. Both spectrometers viewed the capsule from the side, through the tungsten z-pinch plasma. TREX5 acquired data with spatial resolution parallel to the equator and TREX6 acquired data with spatial resolution parallel to the polar axis. The times are with

respect to the foam shock arrival at the axis. The uncertainty in the absolute timing is ± 250 psec at 1σ, since shock measurements were not obtained in the Z1467 experiment.

9. Comparison of post-processed simulations with the spectra obtained in experiment Z1467.

10. Time-resolved spatially-averaged implosion core temperature and density inferred from the Z1467 TREX5 data and from the synthetic spectra obtained by post processing LASNEX simulations of the implosion. The density curves marked with a + and * represent the H-like Ar and He-like Ar results, respectively. The experimental temperature uncertainties are approximately ± 5% and the density uncertainties are ± 25%.

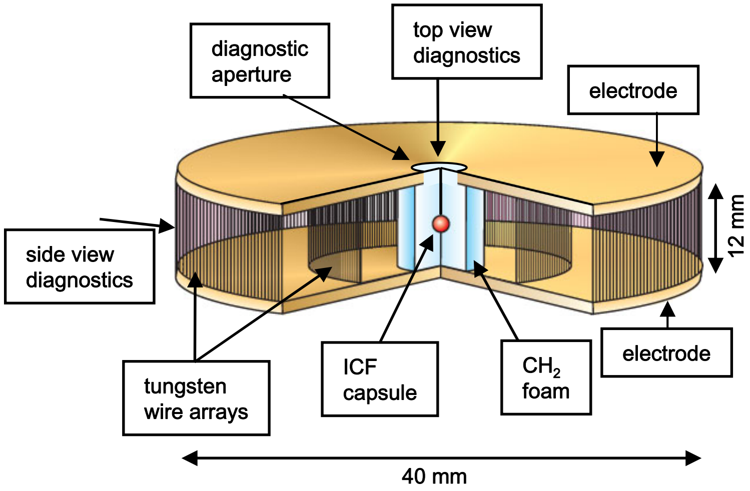

Figure 1; Bailey et al; Physics of Plasmas

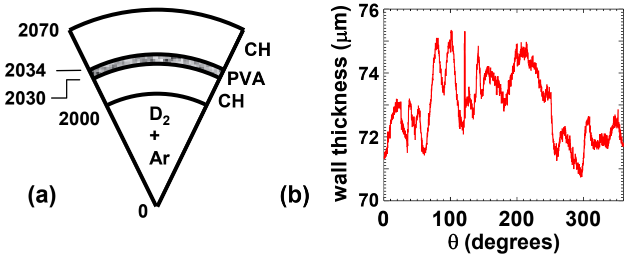

Figure 2; Bailey et al; Physics of Plasmas

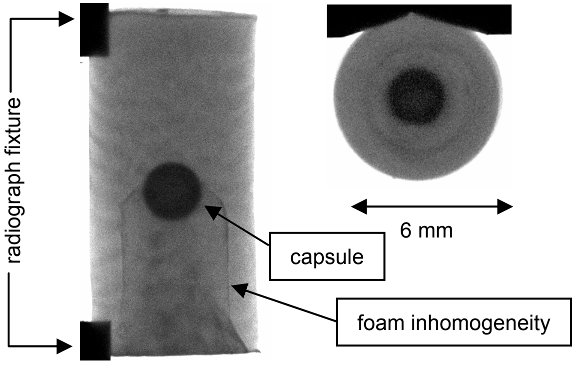

Figure 3; Bailey et al; Physics of Plasmas

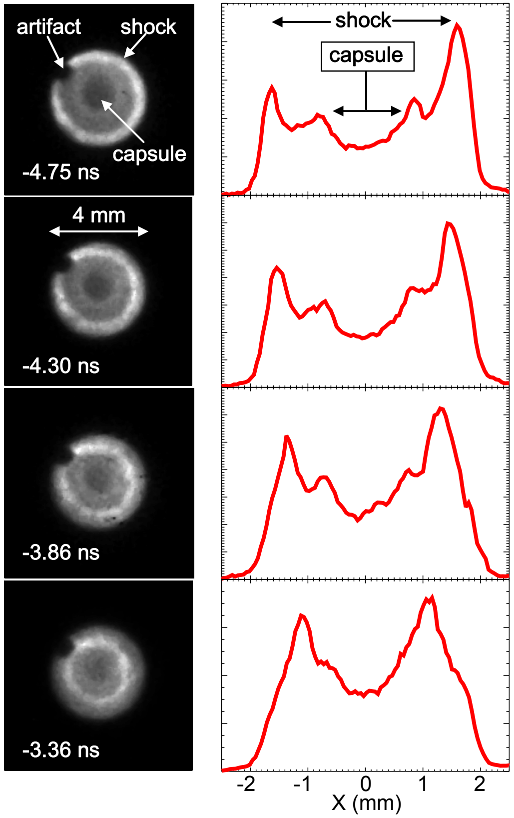

Figure 4; Bailey et al; Physics of Plasmas

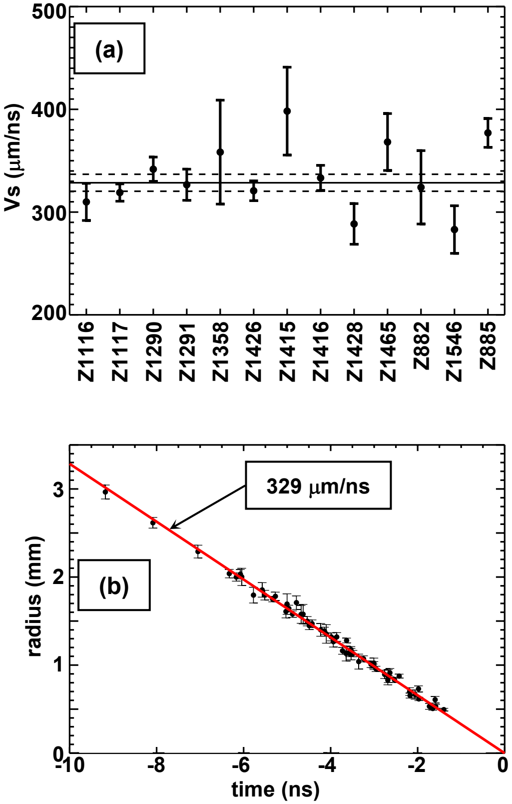

Figure 5; Bailey et al; Physics of Plasmas

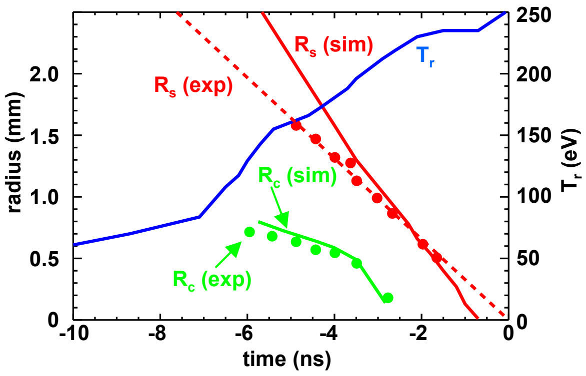

Figure 6; Bailey et al; Physics of Plasmas

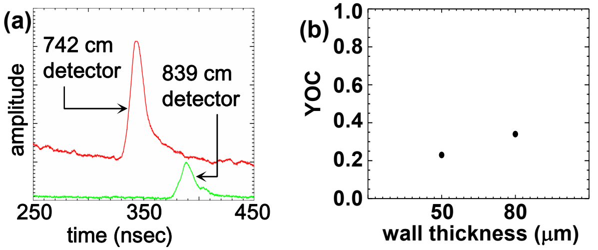

Figure 7; Bailey et al; Physics of Plasmas

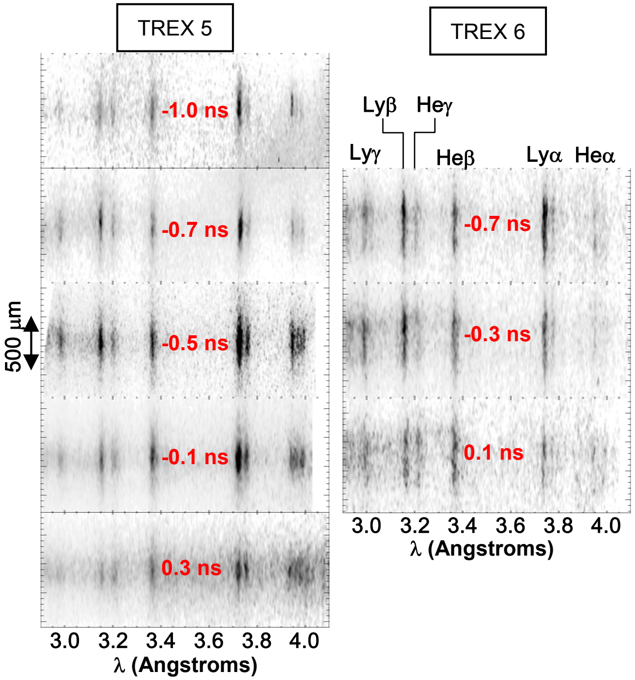

Figure 8; Bailey et al; Physics of Plasmas

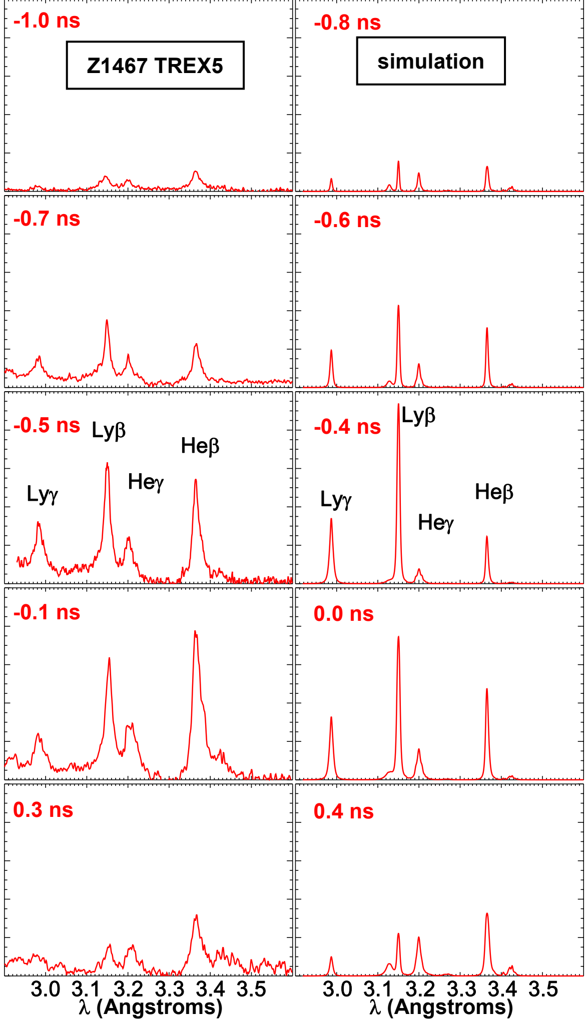

Figure 9; Bailey et al; Physics of Plasmas

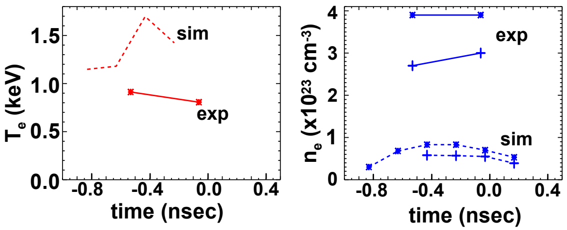

Figure 10; Bailey et al; Physics of Plasmas